

LOADING CAPACITIES OF BONDED COMPOSITE PIPE JOINTS OF DIFFERENT STRUCTURES

G. H. Zhao,^{1,2*} S. H. Hu,¹ and C. Feng^{1,3}

Keywords: basalt-fiber-reinforced polymer (BFRP), inverse analysis, damage evolution, adhesive joint, cohesive zone model (CZM)

Fiber-reinforced composite materials are increasingly used in oil and gas transmission, and joints are the areas prone to failure in pipelines. Damage evolution in the adhesive joints connecting pipes made for basalt-fiber-reinforced polymers (BFRPs) was analyzed. First, finite-element models for three types of adhesive joints (single-lap, sleeve, and scarf ones) were developed. Second, an optimal cohesive zone model (CZM) for the adhesive layer was developed based on the inverse analysis of the results of debonding experiments. Finally, the damage evolution in the adhesive joints was analyzed under internal pressure, tension, bending, and torque, and their pipeline loading capacities were evaluated. Results showed that the single-lap joint exhibited the highest ultimate load-carrying capacity at a unit overlapping length, followed by the sleeve joint, but the scarf joint had the lowest unit ultimate load. For sleeve and scarf joints, the presence of a gap or a weak interface between two pipe adherends led to a reduction in their load-carrying capacity. These findings provide a basis for the design of the composite pipe joints.

1. Introduction

Composite pipes are connected together by joints. Compared with the traditional mechanical joints [1], adhesively-bonded joints have a lighter weight, a uniform stress distribution, good corrosion resistance, and good fatigue performance. However, due to the complex geometry and discontinuous material properties, adhesive joints are often the weakest parts

¹School of Mechanical Engineering, Southwest Petroleum University, Chengdu 610500, P.R. China

²Oil and Gas Equipment Technology Sharing and Service Platform of Sichuan Province, Chengdu 610500, P.R. China

³Hubei Huazhong Optoelectronic Technology Co., Ltd., Xiaogan 432000, P.R. China

*Corresponding author; e-mail: zhaogh@swpu.edu.cn

in composite pipelines. For an adhesively-bonded joint, the failure usually happens in the adhesive layer [2]. Therefore, the load-carrying capacity of pipelines is primarily determined by the bonding performance of the adhesive layer.

For adhesively bonded pipe joints, theoretical investigations were carried out using many simplifications. For example, it was assumed that pipeline components are linearly elastic, stress distributions in the adhesive layer are uniform; two-dimensional models are used, and so on [3]. As a result, the failure evolution in a joint is difficult to obtain. For joints having a complex structure, their properties are usually studied by either experimental or numerical methods. Joint strengths can be measured, and both the failure processes and the morphology after destruction can be observed directly [4-7]. Using finite-element (FE) methods, the damage initiation and failure development can be shown in detail for both adherents and adhesive layer, and the influences of joint structure and material properties on the load-carrying capacity can eventually be revealed [8-10]. These studies were aimed mainly at adhesive joints of flat geometries, but cylindrical adhesive joints have been investigated less.

In numerical simulations of adhesive pipe joints, the von Mises criterion is frequently used, because it is convenient for failure predictions in adhesive layers. Zhang et al. [11] calculated the stress distribution, in a steel riser bonded, by a composite sleeve, under different loads, and the adhesive strength of the sleeve was successfully evaluated. Sulu et al. [12] studied the ultimate internal pressure in an E-GF/epoxy composite pipe bonded by sleeves, and the effects of fiber orientation, sleeve length, and adhesive materials on the joint strength were discussed. Simulating the failure and fracture properties of adhesive joints, Parashar et al. [13] studied the effect of fiber orientation on the fracture toughness of the adhesive layer bonding FRP tubes. Nimje et al. [14] discussed the applications and fracture properties of functionally graded adhesive layers connecting laminated FRP pipes. By means of the Tsai–Wu criterion, Prakash et al. [15] calculated the strength of composite laminated pipes bonded by sleeves and a functionally graded adhesive, and the position of damage initiation was determined.

The reliability of pipe joints has not to be lower than that of the pipe body. For adhesively-bonded joints, a higher strength can be achieved by improving the adhesive structure, enhancing its adhesive property, treating the adhesive surfaces, and so on. Among these methods, the adhesive structure plays the major role, because it determines both the load transfer path and the failure mode.

As a background of applications, the oil and gas transmission is considered in this paper. The damage evolution in frequently used joints, including single-lap, sleeve, and scarf ones, which joins BFRP pipes, is simulated for different basic loads. The influence of joint structures on the load-carrying capacity is evaluated, providing insights for the design of various composite pipe joints.

2. Numerical Model

First, an FE model of a single-lap joint was developed. Then, the optimal cohesive zone model (CZM) for the adhesive layer was created for the adhesive layer based on debonding experiments and an inverse analysis.

2.1. FE model

The mechanical model of a single-lap joint connecting BFRP pipes is illustrated in Fig. 1. The internal pipe is bonded to the external pipe by an overlapping adhesive. Both pipes were 125-mm long. The internal pipe had an outer diameter of 100 mm and a wall thickness of 6 mm. The adhesive layer was 40-mm long and 0.4-mm thick.

One end of the joint was fixed, the other end was free, and a coupling point O was defined on this end face. A tensile load F , bending moment M , and torque T , were applied to the coupling point separately. The internal pressure P operated on the internal surface of the joint. In the following Sections, three types of loads on the joints will be considered. The first type was a 12.8 MPa pressure P , and then a linearly increasing tensile displacement q_z is applied in the

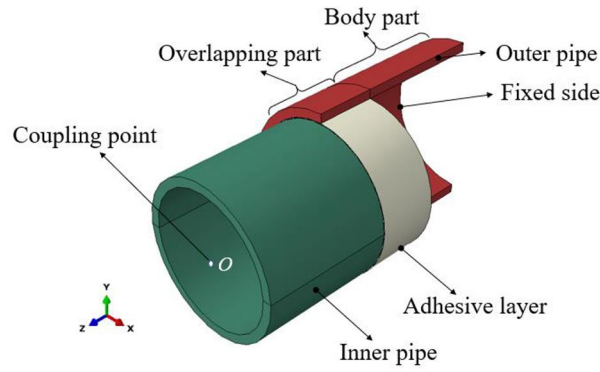


Fig. 1. Sketch of the single-lap joint.

TABLE 1. Properties of the Unidirectional BFRP Laminate and the Araldites 2015 Adhesive

Property			BFRP [16]	Araldites 2015 [17]
Elastic modulus, GPa	Tension	E_{11}	64	1.85
		E_{22}	11	
	Shear	E_{12}	2.5	0.56
		E_{23}	1.4	
Poisson's ratio		μ_{12}	0.33	0.33
Strength, MPa	Tension		1800	21.63
	Compression		1125	
	Shear		39	17.9
	Fracture toughness, N/mm	Tension		-
	Shear		-	4.7

$+z$ -direction. The pressure P is within the normal range of oil and gas gathering pipelines. The second type is bending at an angle θ_x applied in the $+x$ -direction, and the third type is torsional at an angle θ_z applied in the $+z$ -direction.

The internal and external pipes were both made of a BFRP, with the winding sequence $[0/90]_{30}$, and is 0.2-mm-thick layers. The adhesive was an Araldites 2015 epoxy. The mechanical properties of the unidirectional BFRP laminate and the adhesive are listed in Table 1 [16-17], where the subscripts 1, 2, and 3 denote an orthogonal coordinate system with the 1-axis along the fiber direction.

The ABAQUS FE software was used in this study. The joint was divided into 100 finite elements in the circumferential direction. The adherend pipe, which was divided into body and overlapping parts, as shown in Fig. 1, was meshed with 8-node hexahedral solid elements (C3D8R). For the body part, the element sizes in longitudinal and radial directions were 2 mm. For the overlapping part, the mesh was 0.5 mm longitudinally. In the radial direction, the element size was 0.4 mm for the 2-mm-thick layer right next to the adhesive and 2 mm for the rest of 4-mm-thick layer. A 4-mm-thick layer of cohesive COH3D8 elements was adopted to simulate the adhesive layer. The properties of the unidirectional laminate, indicated in Table 1, were assigned to each layer of the pipe according to ply orientations. The traction-separation relationship of the adhesive layer was described by the CZM [18], and the cohesive parameters were found in a debonding experiment on the adhesive.

2.2. CZM of the adhesive layer

The mixed-mode tensile/shear fracture was applied for the adhesive layer. For convenience, the bilinear CZM was used, whose equations are [16, 19]

$$t_j = \begin{cases} \frac{t_j^0}{\delta_j^0} \delta_j & \text{for } 0 < \Delta \leq \delta_j^0, \\ t_j^0 \frac{\delta_j^f - \delta_j}{\delta_j^f - \delta_j^0} & \text{for } \delta_j^0 < \Delta < \delta_j^f, \\ 0 & \text{for } \Delta \geq \delta_j^f, \end{cases} \quad (1)$$

where t^0 and δ^0 are the cohesive strength and the corresponding cohesive separation, respectively, δ^f is the critical separation; the cohesive stiffness k and cohesive energy G are expressed as $k = t^0 / \delta^0$ and $G = t_j^0 \cdot \delta_j^f / 2$. The subscript j ($j = n, s, t$) denote the mutually orthogonal radial and two shearing directions, respectively. Among the parameters t^0 , δ^f , k , and G , any three can determine the CZM [20]. Generally, k , δ^f , and G have a definite physical meaning and are used as the basic cohesive parameters.

Before the damage initiation, the constitutive relationship for the adhesive layer was taken in the form [17]

$$\begin{Bmatrix} t_n \\ t_s \\ t_t \end{Bmatrix} = \begin{bmatrix} k_n & & \\ & k_s & \\ & & k_t \end{bmatrix} \begin{Bmatrix} \delta_n \\ \delta_s \\ \delta_t \end{Bmatrix}. \quad (2)$$

Damage in the adhesive layer occurred when the quadratic nominal stress criterion [21]

$$\left\{ \frac{t_n}{t_n^0} \right\}^2 + \left\{ \frac{t_s}{t_s^0} \right\}^2 + \left\{ \frac{t_t}{t_t^0} \right\}^2 = 1 \quad (3)$$

was satisfied.

Then, the damage variable D ($0 \leq D \leq 1$) was defined as

$$D = \frac{\delta_m^f (\delta_m^{\max} - \delta_m^0)}{\delta_m^{\max} (\delta_m^f - \delta_m^0)}, \quad (4)$$

where $D = 1$ corresponds to failure [22]. In Eq. (4), the quantity $\delta_m^f = 2G_{Mix} / t_m^0$ denotes the equivalent displacement, and the superscript “max” indicates the maximal value [16]. G_{Mix} is the mixed energy release rate, which is determined by the Benzeggagh–Kenane criterion [23]:

$$G_{Mix} = +(G_{IIC} - G_{IC}) \left(\frac{G_{II}}{G_I} \right)^\eta, \quad (5)$$

where the subscripts I and II denote the normal and tangential directions, respectively, G_C is the critical fracture energy, and η is the energy coefficient, taken as 1. After the damage initiates, the stiffness of the adhesive layer gradually degrades and is described as $k_j' = (1 - D)k_j$.

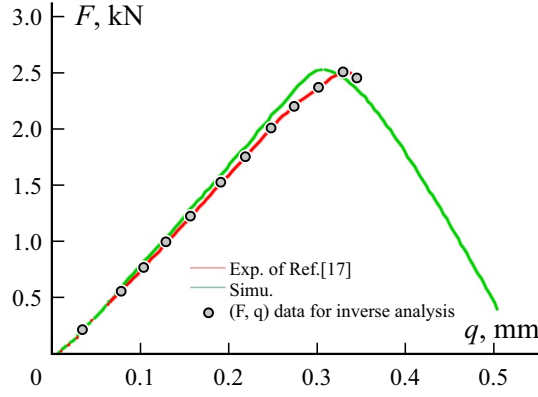


Fig. 2. Test data for the inverse analysis of Araldites 2015 adhesive and results of numerical calculations.

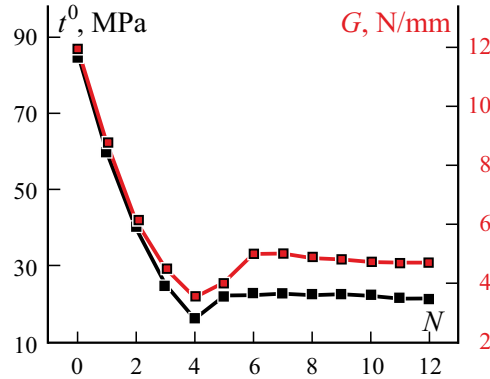


Fig. 3. The cohesive strength t^0 and cohesive energy G vs. iteration number N .

2.3. Inverse analysis

The cohesive parameters of the adhesive layer differ from the material properties described in Table 1. They need to be determined by combined experiments and numerical calculations. In this study, the FE model was developed based on the results of tensile experiments for a single-lap joint [17], and the testing process was simulated. The adhesive layer of the joint specimen was modeled using the aforementioned CZM, and the optimal cohesive parameters were obtained by the inverse analysis using the modified Levenberg–Marquardt (L–M) method [24]. This optimal CZM was then used to study the damage evolution of joints with different structures.

In the tensile experiment on the single-lap joint [23], the dimension of the adherend CFRP plate was $125 \times 15 \times 2.4$ mm, and the Araldite 2015 adhesive layer was 0.2-mm thick and 10-mm long. The tensile test of the joint specimen was performed at room temperature with a loading rate of 0.5 mm/min. The relationship between the load F and displacement q was recorded (Fig. 2), where 12 points (F , q) were chosen for the inverse analysis.

The FE model of the single-lap joint specimen from [17] was developed using the method outlined in Section 2.1. The stiffness k was 10^6 N/mm³, and the initial cohesive parameters $\mathbf{p}^{(0)T} = [G, t^0]$ were chosen as [12 N/mm, 85 MPa], which was several times greater than the fracture toughness and the strength of Araldite 2015, respectively. Employing $\mathbf{p}^{(0)}$ in the CZM of the FE model, the predicted $F - q$ curves were obtained. The difference between the predicted and experimental values were described by an error function Ψ , which determined by the modified L–M method. Then, the Jacobian matrix of Ψ was calculated, and a correction vector $\mathbf{p}^{(0)}$ was derived. Using $\mathbf{p}^{(0)}$, the cohesive parameters were updated as

$\mathbf{p}^{(1)} = \mathbf{p}^{(0)} + \mathbf{p}^{(0)}$. The iterations were continued until the convergence criterion $\sum_{i=1}^n |\rho_i^{(k)}| / \sum_{i=1}^n |p_i^{(k)}| \leq 10^{-6}$ was satisfied, where the $\mathbf{p}^{(k)}$ is the optimal cohesive parameters. For more details of the modified L–M method see [24].

With increasing number of iterative steps of the inverse analysis, the predicted $F-q$ curve approached the experimental curve gradually. Figure 3 shows the variation of t^0 and G with iterations. The optimal cohesive parameters $t^0 = 21.50$ MPa and $G = 4.68$ N/mm were achieved in 12 iterations. Using the optimal cohesive parameters and the meshing method presented in Section 2.1, the tensile test was simulated, and the predicted $F-q$ curve is presented in Fig. 2. It is seen that the predicted curve matches the experimental result very well. Meanwhile, the numerical method was also verified.

For oil and gas pipelines, basic loads include an internal pressure, tension, bending, and torque. Next, the CZM with the optimal cohesive parameters is used to describe the Araldite 2015 adhesive, and the load-carrying capacities of joints with different structures will be evaluated.

3. Single-lap Joint

Single-lap joints are commonly used in pipe-to-pipe connections. In this Section, the damage evolution is simulated under different basic loads, and the evaluation of joint strength is discussed.

3.1. Internal pressure and tension

After loading by the internal pressure $P = 12.8$ MPa, the relationship between the tensile force F and the tensile displacement q_z found is presented in Fig. 4. At the displacement of $q_z = 1.83$ mm, F reached the ultimate value $F_{\max} = 210.07$ kN. At this load, a failure occurred in the adhesive layer, but the BFRP pipe remained in the elastic state. To validate the rationality of the pipe of 125-mm length, a single-lap joint connecting two 250-mm-long pipes was simulated under the same other conditions mentioned above. The ultimate force F_{\max} predicted was 210.59 kN, and the relative error was only 0.25% compared with F_{\max} . Therefore, the pipe of 125-mm length was reasonable, and the boundary conditions had only a small influence on the damage process in the joint.

In Fig. 4, loading points corresponding to $q_z = 1.23, 1.83,$ and 1.91 mm were selected, and the corresponding contours of the damage variable D of the adhesive layer are shown. When q_z increased to 1.23 mm, damage initiated at both ends of the adhesive layer. Along with growing q_z , the damage zones at both ends expanded, and the damage zone extended from the ends to the middle area. When F reached F_{\max} , the failure occurred in the adhesive layer, and the damage zones moved inward. When q_z increased further, F dropped sharply, and the failure zone extended throughout the adhesive layer until the complete destruction. Loaded by both the internal pressure and tension, the single-lap joint failed completely when the failure zone of the adhesive layer developed from the ends up to the middle section. It can be concluded that enhancing the bonding strength of the end adhesive layer is an effective way to improve the load-carrying capacity of the adhesive layer.

3.2. Bending

Variations in the bending moment M for the coupling point at the bending angle θ_x of the loading point are shown in Fig. 5. The maximal value of M was $M_{\max} = 4.8$ kN·m at $\theta_x = 2.13^\circ$. Three characteristic points, $\theta_x = 0.96, 1.48,$ and 2.13° , were selected on the $M-\theta_x$ curve, and the corresponding contours of D are shown in the figure. Along with increasing θ_x , damage initiated on the end of the tensile side, as shown in the contour for $\theta_x = 0.96^\circ$. On increasing θ_x

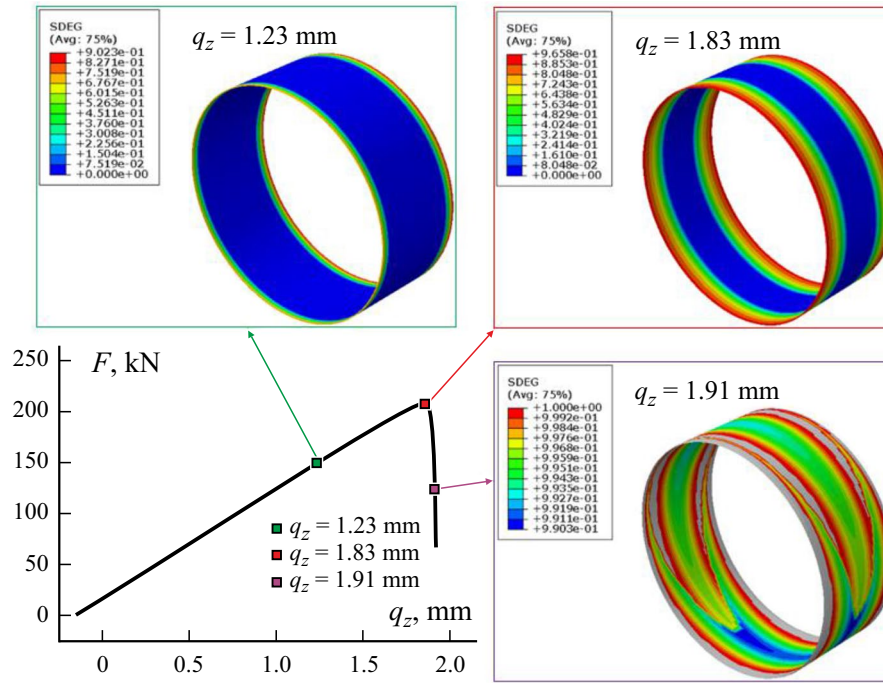


Fig. 4. $F - q_z$ curve of a single-lap joint and contours of the damage variable D for different q_z .

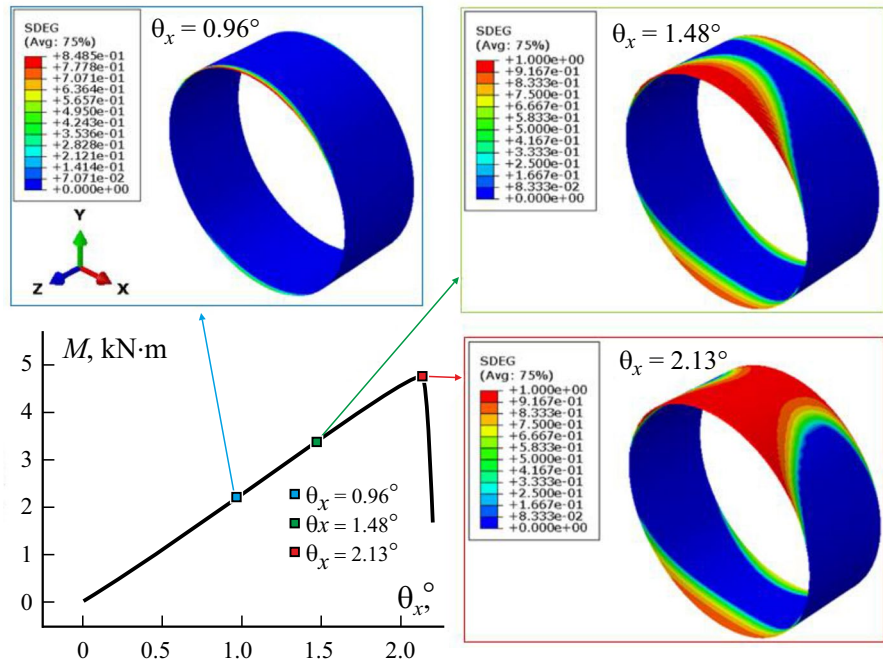


Fig. 5. $M - \theta_x$ curve of a single-lap joint and contours of the damage variable D for different θ_x .

further, the damage area expanded from both ends to the middle, and damage happened at the end of the compressing side, as shown in the contour for $\theta_x = 1.48^\circ$. When the M reached the maximum, the tensile side of the adhesive layer failed completely, but most of the area of the compressing side remained undamaged, except for the area near both ends (see the contour for $\theta_x = 2.13^\circ$). This fact indicated that the joint failure occurred owing to the failure on the tensile side.

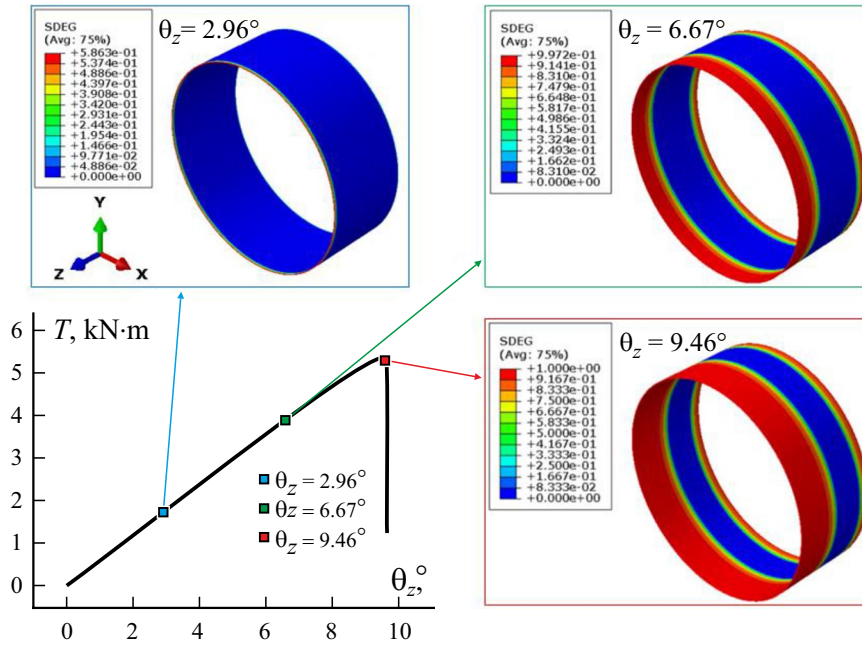


Fig. 6. $T - \theta_z$ curve of a single-lap joint and contours of the damage variable D for different θ_z .

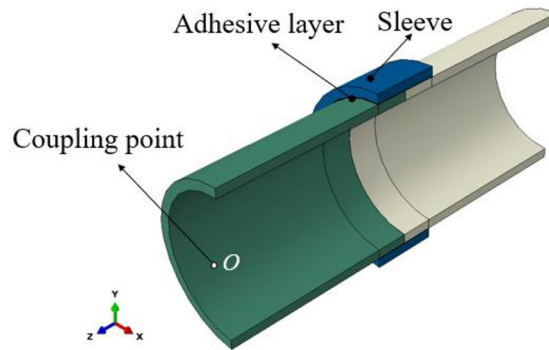


Fig. 7 Sketch of the sleeve joint.

3.3. Torsion

The variation of torque T with θ_z is illustrated in Fig. 6. The maximal torque T_{\max} was 5.31 kN·m at $\theta_z = 9.46^\circ$. Three characteristic points are chosen in the $T - \theta_z$ curve, $\theta_z = 2.96, 6.67,$ and 9.46° , and the corresponding contours of D are shown. The distribution D was axisymmetric. When T grew, damage initiated from the end near the internal pipe, as shown in the contour for $\theta_z = 2.96^\circ$. Subsequently, the other end near the external pipe began to fail. On further growth of θ_z , the damage area developed from both ends towards the middle. The damage area near the internal pipe side extended faster than the other side, as shown in the contour for $\theta_z = 6.67^\circ$. As the torque reached value of T_{\max} , the adhesive layer failed almost completely (as seen in the contour for $\theta_z = 9.46$). The joint collapsed when the failure zone developed from the side near the internal pipe to the entire adhesive layer.

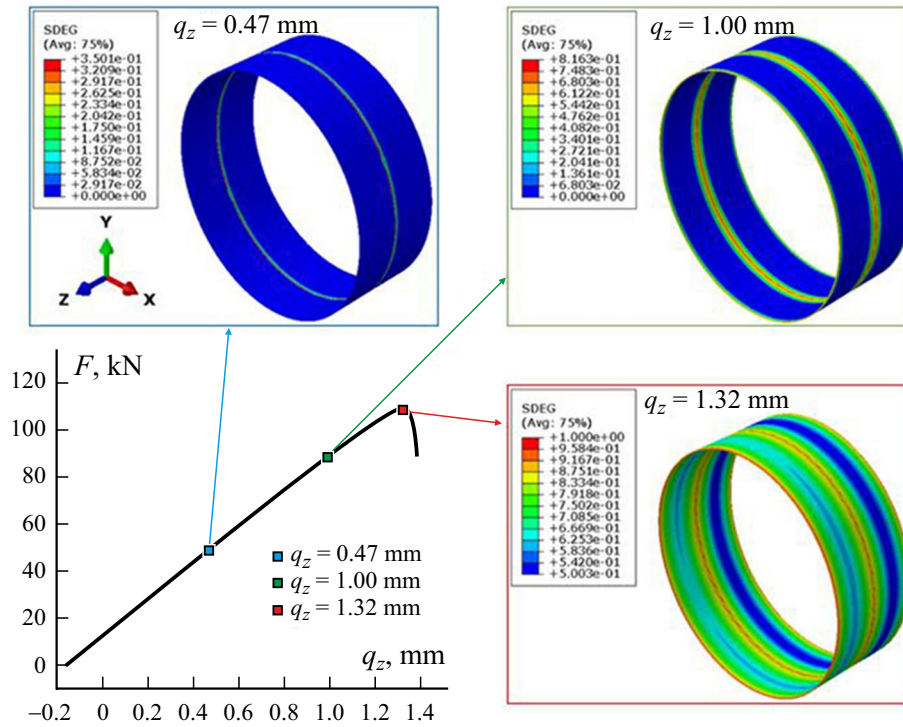


Fig. 8. $F - q_z$ curve of a sleeve joint and contours of the damage variable D for different q_z .

4. Sleeve Joint

In contrast to the prepreg technology commonly used for bonding composite pipe sections of the same diameter, premanufactured sleeve couplers offer a simpler connection process, improve automation and efficiency, and is increasingly utilized in the bonding of composite pipes.

Figure 7 shows a sleeve joint where two pipes are connected by a sleeve and there is no adhesive between the end faces of pipes. Load transmission occurred through the adhesive layer between the internal face of sleeve and the external face of pipes. The pipes had a thickness of 6 mm, an outer diameter of 100 mm, and a $[0/90]_{30}$ layup. Each single layup layer was 0.2-mm thick. The material properties and layup of the sleeve were the same as those of the pipe, and the wall thickness was also 6 mm. The pipes were all 125-mm long. The length and thickness of the adhesive layer were 40 and 0.4 mm, respectively. To simulate the damage evolution, an FE model for the sleeve joint similar to that used for the single-lap joint was created. One its end was fixed, but the other one was loaded by a tensile displacement q_z , bending angle θ_x , and torsion angle θ_z at the coupling point. An internal pressure P was applied to the internal face of the joint.

4.1. Internal pressure P and tension

At $P = 12.8$ MPa, the variation in the tension force F with q_z is shown in Fig. 8. The maximal value F_{\max} was 109.25 kN at $q_z = 1.32$ mm. The loading points at $q_z = 0.47$, 1.00, and 1.32 mm were chosen, and the corresponding contours of damage variable D are also shown in the figure. As q_z increased, damage also appeared on both ends of the adhesive layer (as seen in the contour for $q_z = 1.00$ mm). As F increased further, an asymmetric damage area arose, and the damage level developed more quickly at the left side, which can be seen in the contour for $q_z = 1.32$ mm. This means that a perfect symmetry did not exist, and the sleeve joint failed by debonding of one pipe section.

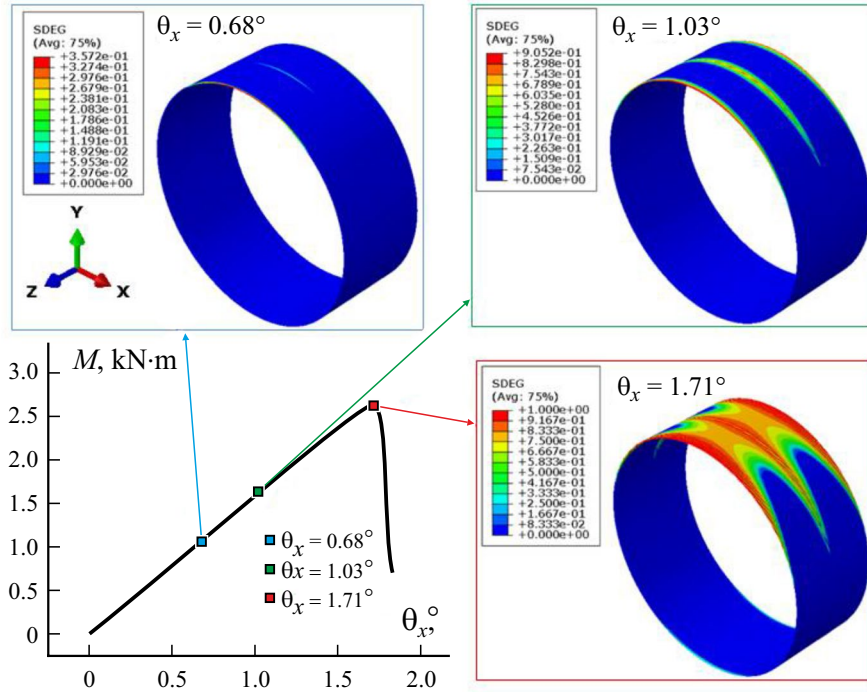


Fig. 9. $M - \theta_x$ curve of a sleeve joint and contours of the damage variable D for different θ_x .

4.2. Bending

The relationship between the bending moment M and the rotation angle θ_x at the loading point is shown in Fig. 9. The maximal moment M_{\max} was 2.63 kN·m at $\theta_x = 1.71^\circ$. Choosing the loading points at $\theta_x = 0.68, 1.03$, and 1.71° in the $M - \theta_x$ curve, the corresponding damage contours were also presented. Damage first occurred on the tensile part of the end section, as shown in the contour at $\theta_x = 0.68^\circ$. Then, the middle section of the tensile part was also damaged (as seen in the contour at $\theta_x = 1.03^\circ$). The bending moment rapidly decreased after reaching $M = M_{\max}$, and complete failure occurred at both ends and the middle section of the tensile side, as shown in the contour at $\theta_x = 1.71^\circ$. Therefore, the sleeve joint collapsed owing to the failure of the tensile side in the adhesive layer.

4.3. Torsion

Figure 10 shows variations in the torque T with torsion angle θ_z , and the maximal torque T_{\max} was 4.64 kN·m at $\theta_z = 11.46^\circ$. Three characteristic points of $\theta_z = 4.04, 6.21$, and 11.46° were chosen in the $T - \theta_z$ curve, and the corresponding contours D are presented in the figure. For $\theta_z = 4.04^\circ$, damage initiated at ends of the adhesive layer. The damage arose in the middle section of the adhesive layer near the gap, and the damage area was divided into two parts by the middle section and extended to the middle of each part, as shown in the contour at $\theta_z = 6.21^\circ$. Finally, the left part of the adhesive layer was destroyed completely (see the contour at $\theta_z = 11.46^\circ$).

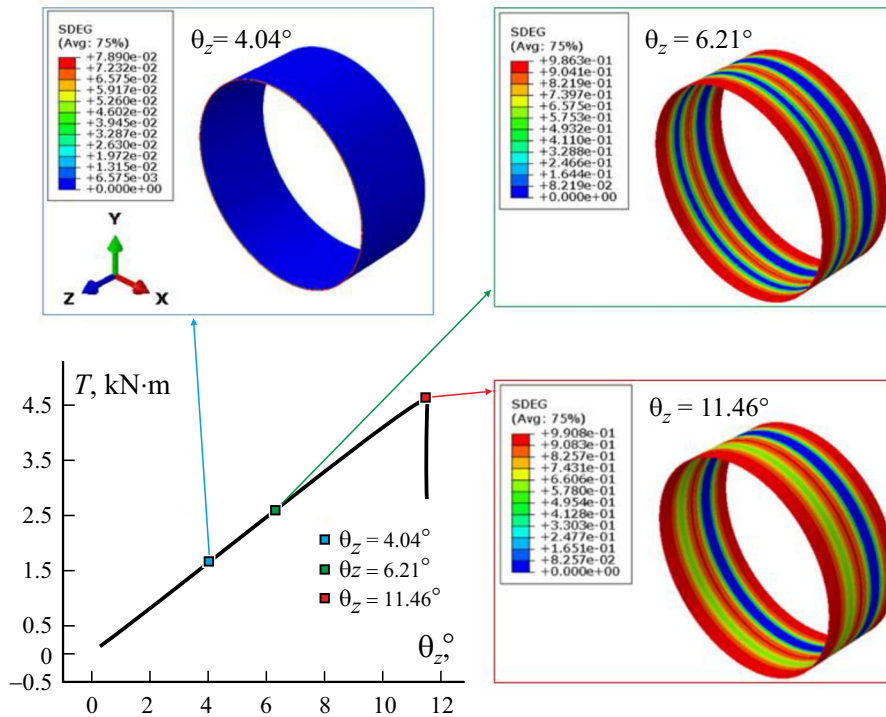


Fig. 10. $T-\theta_z$ curve of a sleeve joint and contours of the damage variable D for different θ_z .

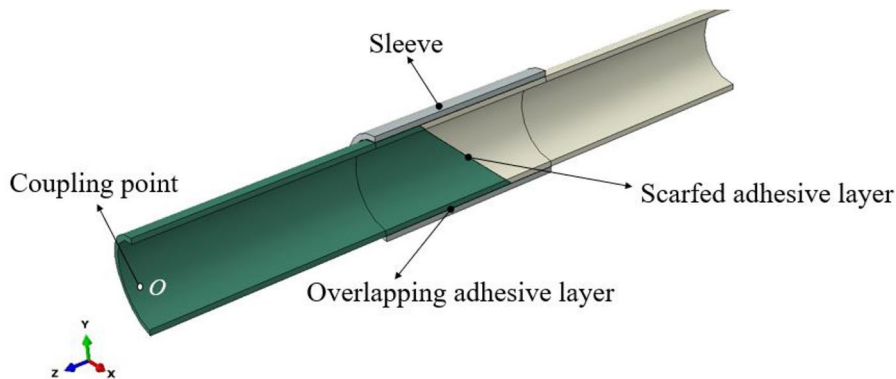


Fig. 11 Sketch of a scarf joint.

5. Scarf Joint

The model of a scarf joint is shown in Fig. 11. The scarf joint is similar to the sleeve joint considered in Section 4, with the only difference that the contacting surface of the two BFRP pipes formed a slope with the Araldites 2015 adhesive. The slope had an angle of 45° on the xz plane, and the scarfed adhesive layer was of 0.5-mm thick. Due to existence of the scarfed adhesive layer, the length of the adherend pipe and the sleeve were chosen to be 350 and 200 mm, respectively. Results showed that the joint was broken due to failure of the overlapping adhesive between the sleeve and pipes, but the scarf adhesive layer was not damaged. The damage evolution in the overlapping adhesive layer will be discussed in detail further.

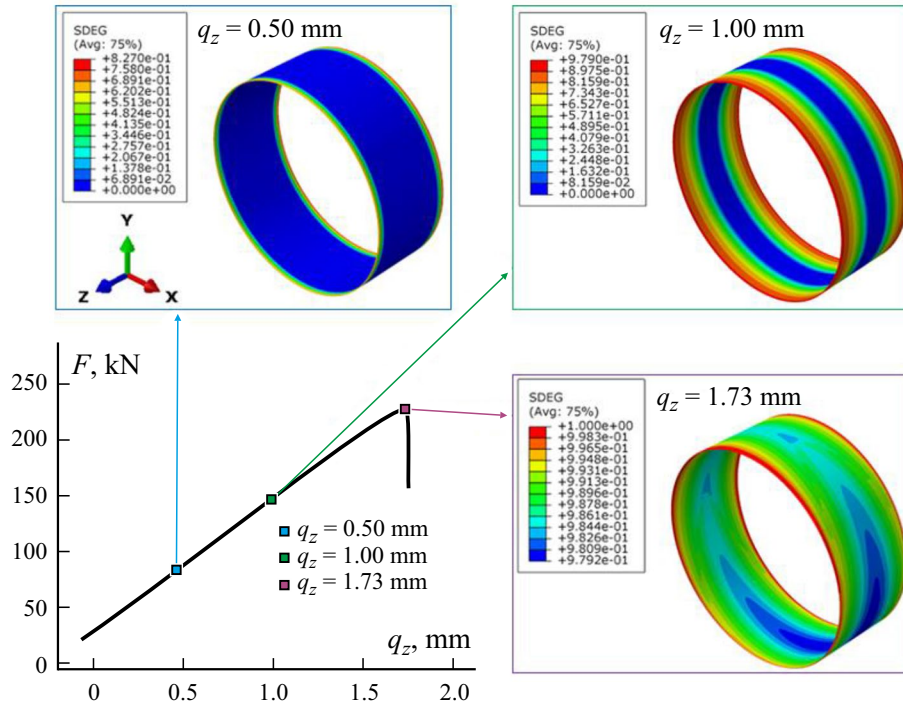


Fig. 12. $F - q_z$ curve of a scarf joint and contours of the damage variable D for different q_z .

5.1. Internal pressure and tension

The variation in the tensile force F with tensile displacement q_z under an internal pressure $P = 12.8$ MPa is presented in Fig. 12. The maximal tension force F_{\max} was 229.65 kN at $q_z = 1.73$ mm. Choosing characteristic loading points at $q_z = 0.50$, 1.00, and 1.73 mm, the corresponding contours D of damage variable are shown in Fig. 12. At $q_z = 0.50$ mm, damage initiated at both ends of the adhesive layer, as shown in the contour D . When q_z increased to 1.00 mm, D on the ends became close to 1, and the damage area moved from the ends towards the middle section. For the ultimate tension F_{\max} , both ends failed completely, as shown in the contour at $q_z = 1.73$ mm. Then, the load-carrying capacity of the joint sharply decreased until the complete failure.

5.2. Bending

For a scarf joint, the variation in the bending M with the rotation angle θ_x of the loading point is shown in Fig. 13. The maximal bending moment M_{\max} was 5.23 kN·m at $\theta_x = 2.02^\circ$. The loading points $\theta_x = 0.50$, 1.08, and 2.02° were chosen in the $M - \theta_x$ curve, and the corresponding contours D are shown in the figure. Damage initiated at ends of the tensile part as shown in the contour at $\theta_x = 0.5^\circ$. Due to the lower stiffness of the scarfed adhesive layer compared with that of the pipe, the load transfer capacity of the scarfed adhesive was weak. As a result, damage also occurred on the middle section of the overlapping adhesive layer at a smaller θ_x , as shown in the contour at $\theta_x = 1.08^\circ$. As θ_x increased further, the damage zone extended more and more on the tensile side of the layer. When M reached M_{\max} at $\theta_x = 2.02^\circ$, the complete failure occurred at both the ends and the middle section of the tension side, but the compressed side remained undamaged.

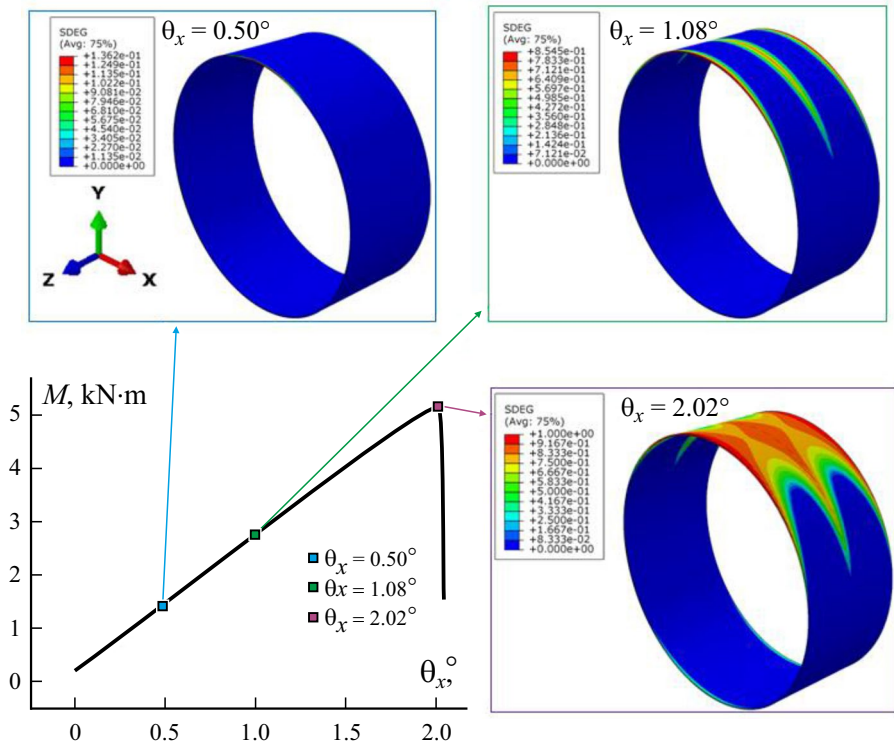


Fig. 13. $M-\theta_x$ curve of a scarf joint and contours of the damage variable D for different θ_x .

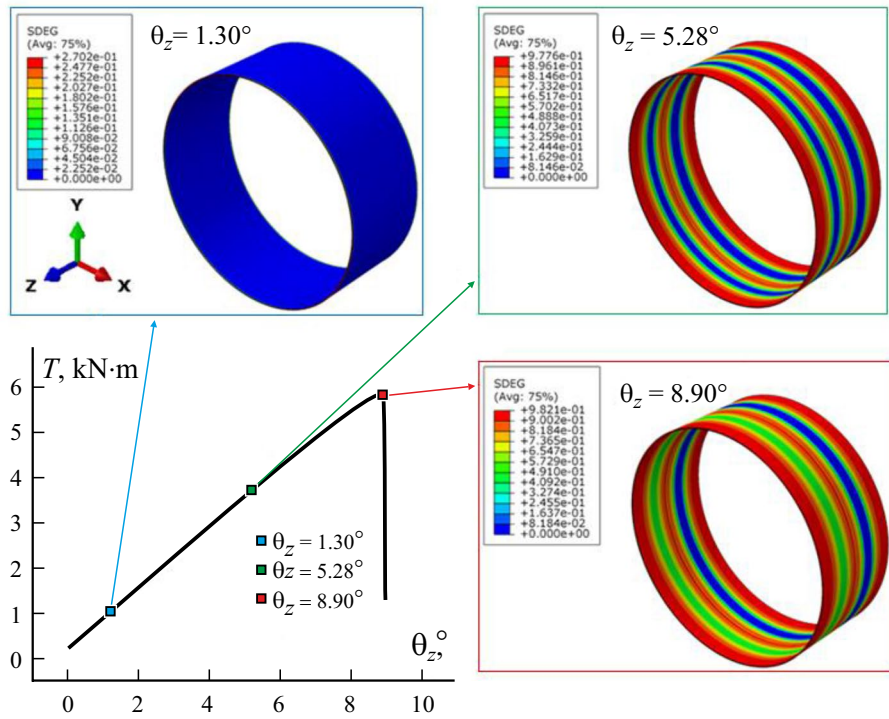


Fig. 14. $T-\theta_z$ curve of a scarf joint and contours of the damage variable D for different θ_z .

TABLE 2. Comparison of Loading Capacities of Joints

Joint type	Ultimate load for unit overlapping length		
	Tension, kN/m	Bending, kN	Torsion, kN
Single-lap joint	5268	120	133
Sleeve joint	2731	66	116
Scarf joint	1145	26	29

5.3. Torsion

The variation in the torque T with torsion angle θ_z is shown in Fig. 14. T_{\max} was 5.834 kN·m at $\theta_z = 8.90^\circ$. Three points in the $T - \theta_z$ curve, at $\theta_z = 1.30, 5.28,$ and 8.90° , the contours of D for the points are also shown in Fig. 14. At $\theta_z = 1.30^\circ$, damage initiated on both ends of the adhesive layer, as shown in the contour of D . With increasing θ_z , damage also happened in the middle section, and the damage zone extended from both layer ends and center (see the contour at $\theta_z = 5.28^\circ$). Owing to the effect of the scarfed adhesive layer, the damage area of the overlapping adhesive layer evolved asymmetrically along the axial direction, as shown in the contour at $\theta_z = 8.90^\circ$. When T sharply decreased, the joint failed completely.

6. Comparison of Load-Carrying Capacities

Table 2 summarizes the ultimate loads for the unit overlapping length, denoted as the unit ultimate load of sing-lap, sleeve, and scarf joints with a scarfed angle of 45° . It is seen that the single-lap joint had the highest unit ultimate loads, followed by those of the sleeve joint. The scarf joint had the lowest unit ultimate loads. For the single-lap joint, the load was transferred from one pipe to another directly by the overlapping adhesive layer. For the sleeve and scarf joints, the load exerted on one pipe was first transferred to the sleeve, and then to another pipe, because there was a gap or weak interface between the two adherend pipes, which lowered the load-carrying capacity.

7. Conclusion

- Based on the results of a debonding experiment on the Araldites 2015 adhesive and the inverse analysis, an optimal cohesive zone model was constructed for studying the load-carrying capacities of adhesive joints.
- For the single-lap joint, failure occurred at the internal pressure and tension, because the damage area of the adhesive layer extended from joint ends towards the middle section along the axial direction. Under the bending moment, the single-lap joint collapsed owing to failure of the adhesive layer on the tensile side. In the torsional loading, the joint failed when the damage of the adhesive layer expended longitudinally from one end near the internal pipe to the other end.
- The sleeve joint had a gap between two pipes, leading to the damage initiation not only at pipe ends but also in the middle section of the adhesive layer. The damage zone was divided into two parts and developed separately when the load increased until complete failure.
- In the scarf joint, failure occurred owing to the damage of the overlapping adhesive layer under the internal pressure-tension, bending, or torque. The lower stiffness of the adhesive layer compared with that of the pipe body resulted in damage initiation on the middle section of the adhesive layer in bending and torque loadings.
- Among the three types of joints investigated, the single-lap joint demonstrated the highest load-carrying capacity at the unit overlapping length, followed by the sleeve joint. The scarf joint exhibited the lowest unit ultimate load. The ends of

the overlapping adhesive layer consistently were the locations of damage initiation under various loads. Therefore, improving the bonding strength at both ends of the adhesive layer is an effective method to enhance the overall strength of such joints.

REFERENCES

1. A. V. Malakhov, A. N. Polilov, and D. Li, et al., "Increasing the bearing capacity of composite plates in the zone of bolted joints by using curvilinear trajectories and a variable fiber volume fraction," *Mech. Compos. Mater.*, **57**, No. 3, 287-300 (2021).
2. A. S. Chepurnenko, S. V. Litvinov, and S. B. Yazyev, "Combined use of contact layer and finite-element methods to predict the long-term strength of adhesive joints in normal separation," *Mech. Compos. Mater.*, **57**, No. 3, 349-360 (2021).
3. M. Shishesaz and S. Tehrani, "The effects of circumferential voids or debonds on stress distribution in tubular adhesive joints under torsion," *J. Adhes.*, **96**, No. 16, 1396-1430 (2020).
4. J. X. Na, W. L. Mu, G. F. Qin, et al., "Effect of temperature on the mechanical properties of adhesively bonded basalt FRP-aluminum alloy joints in the automotive industry," *Int. J. Adhes. Adhes.*, **85**, 138-148 (2018).
5. P. N. B. Reis, J. R. L. Soares, A. M. Pereira, et al., "Effect of adherends and environment on static and transverse impact response of adhesive lap joints," *Theor. Appl. Fract. Mech.*, **80**, 79-86 (2015).
6. B. Andrade, J. P. B. Souza, J. M. L. Reis, et al., "A temperature-dependent global failure criterion for a composite/metal joint," *Compos., Part B*, **137**, 278-286 (2018).
7. H. B. Li, X. M. Zhang, D. T. Qi, et al., "Failure analysis of the adhesive metal joint bonded on anticorrosion plastic alloy composite pipe," *Eng. Fail. Anal.*, **47**, 49-55 (2015).
8. S. V. Kotomin, I. M. Obidin, and E. A. Pavluchkova, "Adhesive bond strength calculation of reinforcing fibers with polymers by the "Loop" method," *Mech. Compos. Mater.*, **58**, 141-150 (2022).
9. J. X. Zhang, Q. H. Qin, Y. Yang, et al., "Dynamic response of foam-filled rectangular tubes subjected to low-velocity impact," *Int. J. Appl. Electromagn. Mech.*, **59**, No. 4, 1441-1449 (2019).
10. J. Panta, A. N. Rider, J. Wang, et al., "High-performance carbon nanofiber reinforced epoxy-based nanocomposite adhesive materials modified with novel functionalization method and triblock copolymer," *Compos., Part B*, **249**, 110401 (2023).
11. Y. Zhang, M. L. Duan, Y. Wang, et al., "Analytical study of the strength of adhesive joints of riser pipes," *Ships. Off-shore. Struct.*, **10**, No. 5, 545-553 (2015).
12. I. Y. Sulu and S. Temiz, "Failure and stress analysis of internal pressurized composite pipes joined with sleeves," *J. Adhes. Sci. Technol.*, **32**, No. 8, 816-832 (2018).
13. A. Parashar and P. Avinash, "Failure mechanism in adhesively bonded FRP pipe sections with different fibre architecture," *Compos., Part B*, **47**, 102-106 (2013).
14. S. V. Nimje and S. K. Panigrahi, "Effects of functionally graded adhesive on failures of socket joint of laminated FRP composite tubes," *Int. J. Damage Mech.*, **26**, No. 8, 1170-1189 (2017).
15. C. Prakash and V. Kumar, "Investigation of functionally graded adherents on Failure of socket joint of FRP composite tubes," *Mater.*, **14**, No. 21, 6365 (2021).
16. T. Li, G. H. Zhao, G. L. Zhang, et al., "Study on progressive damage performance of basalt-fiber wound composite tube," *Polym. Compos.*, **43**, No. 11, 7977-7991 (2022).
17. R. D. S. G. Campilho, M. D. Banea, J. A. B. P. Neto, et al., "Modelling adhesive joints with cohesive zone models: effect of the cohesive law shape of the adhesive layer," *Int. J. Adhes. Adhes.*, **44**, 48-56 (2013).
18. D. Li, Q. S. Yang, X. Liu, et al., "Experimental and cohesive finite element investigation of interfacial behavior of CNT fiber-reinforced composites," *Compos., Part A*, **101**, 318-325 (2017).
19. G. H. Zhao, J. Li, Y. X. Zhang, et al., "An inverse analysis-based optimal selection of cohesive zone model for metallic materials," *Int. J. Appl. Mech.*, **10**, No. 2, 1850015 (2018).

20. P. F. Liu, Z. P. Gu and Z. H. Hu, "Revisiting the numerical convergence of cohesive-zone models in simulating the delamination of composite adhesive joints by using the finite-element analysis," *Mech. Compos. Mater.*, **52**, No. 5, 651-664 (2016).
21. D. D. Chen, G. Y. Sun, M. Z. Meng, et al., "Flexural performance and cost efficiency of carbon/basalt/glass hybrid FRP composite laminates," *Thin. Wall. Struct.*, **142**, 516-531 (2019).
22. H. P. Zhang, H. B. Ding, and A. Rahman, "Effect of asphalt mortar viscoelasticity on microstructural fracture behavior of asphalt mixture based on cohesive zone model," *J. Mater. Civil Eng.*, **34**, No. 7, 4022122 (2022).
23. M. L. Benzeggagh and M. Kenane, "Measurement of mixed-mode delamination fracture toughness of unidirectional glass/epoxy composites with mixed-mode bending apparatus," *Compos. Sci. Technol.*, **56**, No. 4, 439-449 (1996).
24. X. Chen, X. M. Deng, M. A. Sutton, et al., "An inverse analysis of cohesive zone model parameter values for ductile crack growth simulations", *Int. J. Mech. Sci.*, **79**, 206-215 (2014).